Stall cell prediction using a lifting-surface model

Frédéric Plante, Éric Laurendeau, Julien Dandois

Stall cell prediction using a lifting-surface model

Frédéric Plante* Éric Laurendeau†
Polytechnique Montréal, Montréal, Québec, H3T 1J4, Canada

Julien Dandois ‡
DAAA, ONERA, Université Paris Saclay, 8 rue des Vertugadins, 92190 Meudon, France

This paper investigates the use of a lifting surface method towards the study of lift cells on wings, thereby extending the lifting-line model proposed by Spalart. In particular, calculations are made with a 3D Vortex-Lattice Method (VLM) coupled with two-dimensional sectional lift versus angle of attack polar to include viscous effects. This viscous coupling allows to capture pre- and post-stall regimes, making it a Non-Linear Vortex Lattice Method (NL-VLM). Canonical cases are examined, such as infinite span wings and wings with elliptical lift distributions coupled with manufactured lift-curves. To achieve these goals, numerical artifacts are developed. One is to enable solutions over infinite span wings, while the other has been traditionally used to stabilise the numerical scheme in the form of added numerical dissipation. Various parametric studies are performed using Spalart's model and our proposed NL-VLM model. This paper identifies the limitations of both models. As found by Spalart, the lifting line mode suffers from robustness issues without the addition of a Gaussian filter, and the number of cells increases with the number of modes. In contrast the NL-VLM model converges with and without the use of artificial dissipation, without affecting the number of stall cells.

I. Nomenclature

A, B	=	coefficients of the Fourier series of the circulation
$A_{i,j}$	=	coefficients of the VLM influence matrix
$A'_{i,j}$	=	coefficients of the modified VLM influence matrix
b	=	wing span (m)
c	=	chord (m)
c_f	=	Gaussian filter width
C_l	=	lift coefficient
C_{l_α}	=	derivative of C_l with respect to α
$C_{l_{inv}}$	=	inviscid lift coefficient
$C_{l_{vis}}$	=	viscous lift coefficient
k_0	=	wavenumber
N	=	number of mesh panels
$\vec{n}$	=	normal vector
n_i	=	number of chordwise panels
n_j	=	number of spanwise panels
P	=	VLM collocation point
$\vec{q}$	=	velocity induced by a vortex segment ($m \cdot s^{-1}$)
$\vec{r}$	=	distance vector (m)
S_{ref}	=	reference surface (m^2)
T	=	spanwise period
$\vec{V}_\infty$	=	freestream velocity ($m \cdot s^{-1}$)
w	=	downwash velocity ($m \cdot s^{-1}$)
y	=	spanwise coordinate (m)

*Ph.D. Candidate, Department of Mechanical Engineering, frederic.plante@polymtl.ca
†Professor, Department of Mechanical Engineering, eric.laurendeau@polymtl.ca, Senior Member AIAA
‡Research Engineer, Department of Aerodynamics, Aeroelasticity and Acoustics, julien.dandois@onera.fr

α = angle of attack
α_{3D} = geometrical angle of attack
α_{eff} = effective angle of attack
α_i = induced angle of attack
α_{inv} = inviscid angle of attack
α_t = twist angle
$\Delta\alpha$ = angle of attack correction
Δy = spanwise grid spacing (m)
ϵ = convergence tolerance
Γ = circulation
ϕ = velocity potential
λ = aspect ratio b^2/S_{ref}
λ_t = twist period
μ = artificial viscosity coefficient
ω = relaxation factor
ϕ = velocity potential

II. Introduction

Three-dimensional flow features over wings in stall conditions have been experimentally observed since the 1970's. Experiments such as those of Moss and Murdin [1] and Gregory et al. [2] showed three-dimensional vortex structures on essentially two-dimensional wings spanning the entire wind tunnel width. This phenomenon was later studied by Winkelmann and Barlow [3] on a wing based on the Clark Y airfoil with free tips. This experiment showed "mushroom" shaped flow structures over the entire span of the wing and an increasing number of these structures when the aspect ratio of the wing increases. This phenomenon is now often called stall cells. Observations similar to the one of Winkelmann and Barlow [3] were made by Schewe [4]. The number of stall cells increases with the aspect ratio of the wings. Early studies speculated that the wind tunnel walls were responsible for these three-dimensional effects. However, the observation of stall cells over the full span of high aspect ratio wings and wings with free tips discarded the effect of the wind tunnel walls as the origin of stall cells. Experiments by Broeren and Bragg [5] investigated the effect of the type of stall on the three-dimensional stall features. Their results suggest that a trailing edge type of stall is a necessary condition for the appearance of these features. Other experiments by Dell'Orso and Amitay [6] showed an effect of the Reynolds number on the stall cells and identified a transition between a two-dimensional stall to a three-dimensional one with increasing Reynolds number.

This phenomenon has been observed in multiple numerical studies. Manni el al. [7] carried out Unsteady-Reynolds-Averaged Navier-Stokes (URANS) simulations and Delayed Detached Eddy simulations (DDES) of a wing of aspect ratio 10 at a Reynolds number of one million. Bertagnolio [8] obtained stall cells over a wind turbine airfoil with URANS simulations. A previous study by the authors [9] studied the stall cells over a NACA4412 airfoil at a Reynolds number of 350 000 and several sweep angles with URANS simulations, showing the convection of the stall cells on swept wings. All these numerical studies point out the occurrence of stall cells without the application of any three-dimensional disturbance from the geometry. This suggests that the stall cells are caused by an inherent flow instability and not the boundary conditions.

Explanation of the stall cells as a globally unstable mode was proposed by Kitsios et al. [10], Rodriguez and Theofilis [11], He et al. [12] and Zhang and Samtaney [13] for wings at a Reynolds number of a few hundreds to a thousand. A similar study was carried out by Plante et al. [14] for wings based on the NACA4412 airfoil at an intermediate Reynolds number of 350 000 with RANS modeling, for which a trailing edge stall behavior is observed. This study showed that the stall cells predicted with a global stability analysis closely matched the prediction of the non-linear URANS equations in [9].

An attempt to model the stall cells, or lift cells, was done by Spalart [15] using the lifting line theory coupled with a manufactured sectional lift polar including a post-stall regime. This model will be further discussed in this paper. From this model the stall cells can be linked to a negative slope in the $C_l(\alpha)$ curve. Such a conclusion was also reported in the work of Gross et al. [16] where a criterion for the wavelength of the cells was proposed based on the lifting line theory. The model of Spalart [15] included a free parameter in the form of a Gaussian filter width. This numerical element was required to prevent the model from producing very high wavenumber modes. This study [15] suggests a simple inviscid model can be used to explain the stall cells phenomenon and Spalart [15] proposed that a lifting surface model would be

the next level of approximation. Filling this gap is one of the objectives of the present paper.

The lifting line model of Spalart [15] can be described as a Γ-based coupling since it proceeds by assuming a circulation distribution allowing to compute the downwash for each wing station and the induced angle of attack. This induced angle of attack is used to get the viscous lift coefficient of the wing sections. Finally, a new circulation distribution is obtained with the Kutta-Joukowski theorem. This procedure is carried out until the solution reaches steady state. A method of this type was also presented by Chattot [17].

Another approach is to use a α-based method such as the one of van Dam [18]. This method solves the lifting line theory and the viscous effects are taken into account by a correction to the local angle of attack. Extension to this method was presented by Gallay and Laurendeau [19] for an application as a preliminary design tool [20]. Solutions presenting features similar to stall cells were obtained by Gallay and Laurendeau [19]. Similar solutions have also been obtained with a coupling using a decambering approach by Paul and Gopalarathnam [21].

This paper aims to provide the next level of approximation to the lifting line model of Spalart [15], a lifting surface model. It also characterizes the post-stall solutions obtained with a lifting surface model coupled with a viscous database by an α-based method. The paper first presents the numerical methods used in this paper. The lifting line model of Spalart [15] is recalled and the lifting surface model is introduced. A numerical procedure to include a periodicity condition in the lifting surface model is also proposed. Section IV presents the verification of the models. Then, the analyses of post-stall cases with the lifting line and lifting surface models are presented. The cases of infinite wings, elliptic wings and rectangular wings are studied. Results for several aspect ratios and viscous lift polars are presented and the effect of adding a numerical dissipation proposed by Gallay and Laurendeau [19] to the coupling is investigated.

III. Methodology

An inviscid, irrotational, and incompressible flow can be modeled by Laplace's equation :

$$\nabla^2 \phi = 0 \tag{1}$$

with ϕ the velocity potential. Since this equation is linear, solutions can be sought in the form of the superposition of elementary solutions (vortices, sinks, sources, doublets, etc.). A wide variety of methods were developed based on this concept, of which the lifting line and lifting surface models.

A. Non-linear lifting line model

Spalart [15] proposed a model based on the lifting line theory for what he called lift cells. In the present study, numerical experiments with this model are carried out and a lifting surface model will be compared to it. Hence the model for an infinite wing is recalled here. The problem is formulated using a Fourier transform for the circulation Γ :

$$\Gamma(y) = cV_\infty \sum_{j=0}^{\infty} A_j cos(jk_0 y) + B_j sin(jk_0 y) \tag{2}$$

where y is the spanwise coordinate, k_0 the wavenumber, c the wing chord and V_∞ the freestream velocity. The downwash velocity is :

$$w(y) = -\frac{k_0 cV_\infty}{4} \sum_{j=0}^{\infty} jA_j cos(jk_0 y) + jB_j sin(jk_0 y) \tag{3}$$

The circulation is related to the lift coefficient using the Kutta-Joukowsky relation :

$$\Gamma(y) = c\frac{V_\infty}{2} C_l(\alpha_{eff}) \tag{4}$$

and under the small angle hypothesis :

$$\alpha_{eff}(y) = \alpha + \frac{w(y)}{V_\infty} \tag{5}$$

To solve this model one can first assume a distribution for the Fourier coefficients A and B. This allows to compute the downwash distribution and the effective angle of attack. In return this gives the circulation by interpolating the

lift coefficient $C_l(\alpha_{eff})$ in a user given polar and applying the Kutta-Joukowski relation. Finally, the new A and B coefficients can be obtained by the inverse Fourier transform :

$$A_j = \frac{k_0}{\pi c V_\infty} \int_0^{2\pi/k_0} \Gamma(y) cos(jk_0 y) dy \tag{6}$$

$$B_j = \frac{k_0}{\pi c V_\infty} \int_0^{2\pi/k_0} \Gamma(y) sin(jk_0 y) dy \tag{7}$$

The model is then iterated up to the point where the solution reaches a steady state. Spalart proposed to apply a Gaussian filter to the inverse Fourier transform so that :

$$A_j = \frac{k_0}{\pi c V_\infty} e^{-(c_f c j k_0)^2} \int_0^{2\pi/k_0} \Gamma(y) cos(jk_0 y) dy \tag{8}$$

$$B_j = \frac{k_0}{\pi c V_\infty} e^{-(c_f c j k_0)^2} \int_0^{2\pi/k_0} \Gamma(y) sin(jk_0 y) dy \tag{9}$$

where c_f is the filter width. This filter reduces the amplitude of the high wavenumber and has the effect of smoothing out the distribution of the circulation. However, this also means that two values of the circulation and thus of the lift coefficient are obtained simultaneously. The first one is obtained from equation 4 with the lift coefficient interpolated in the lift polar and the other is the one obtained from equation 2. This will be analyzed in section V.A.

B. Lifting surface model - Vortex Lattice Method

Another approach to solve the Laplace's equation is the Vortex Lattice Method (VLM), which is a well known lifting surface model. This method uses vortex ring elements [22] to model a lifting surface and the velocity induced at a point P by a segment of a vortex ring is given by the Biot-Savart equation :

$$\vec{q}_{1,2} = \frac{\Gamma}{4\pi} \frac{\vec{r}_1 \times \vec{r}_2}{|\vec{r}_1 \times \vec{r}_2|^2} r_0 \cdot \left(\frac{\vec{r}_1}{|\vec{r}_1|} - \frac{\vec{r}_2}{|\vec{r}_2|} \right) \tag{10}$$

The numerical setup is shown in fig. 1. The wing is meshed with a structured grid of n_i by n_j cells ($N = n_i \times n_j$ cells) and every line segment of the grid is a vortex segment of intensity Γ_i and the wake is meshed with a vortex ring of semi-infinite length. The latter has the same circulation as the last chordwise vortex ring. The model is closed with a boundary condition to impose a velocity tangential to the lifting surface and one solves for the circulations Γ. This result in a linear system of equation of the form :

$$\begin{bmatrix} A_{1,1} & A_{1,2} & \dots & A_{1,N} \\ A_{2,1} & A_{2,2} & \dots & A_{2,N} \\ \vdots & \vdots & \ddots & \vdots \\ A_{N,1} & A_{N,2} & \dots & A_{N,N} \end{bmatrix} \begin{pmatrix} \Gamma_1 \\ \Gamma_2 \\ \vdots \\ \Gamma_N \end{pmatrix} = -\vec{V}_\infty \cdot \vec{n} \tag{11}$$

with $A_{a,b}$ the influence coefficient for the velocity induced on the panel a by the panel b. The influence of the semi-infinite trailing vortex are added to the influence of the trailing edge vortex ring since it has the same circulation. As such the matrix $\boldsymbol{A}$ is square. This method is suitable for simulation of finite span wings. In order to eliminate the effect of the wing tip, one can carry out the simulations on a very large aspect ratio wing. However, the stall cells have an aspect ratio of the order of the chord length. Hence, meshing a wing of a large aspect ratio with a small spanwise resolution results in a large number of mesh cells. Since the cost of the VLM simulation increases with the square of the number of mesh cells the cost of such simulations can become computationally prohibitive. For this reason, an assumption of periodicity is proposed. To do so, a wing of very large aspect ratio is assumed and the values of Γ are taken to be periodic with a period T meshed with n_j spanwise panels. Hence :

$$\Gamma_{(kn_j+j)n_i+i} = \Gamma_{jn_i+i} \tag{12}$$

with $k \in]-\infty, \infty[$. This is illustrated in fig. 2

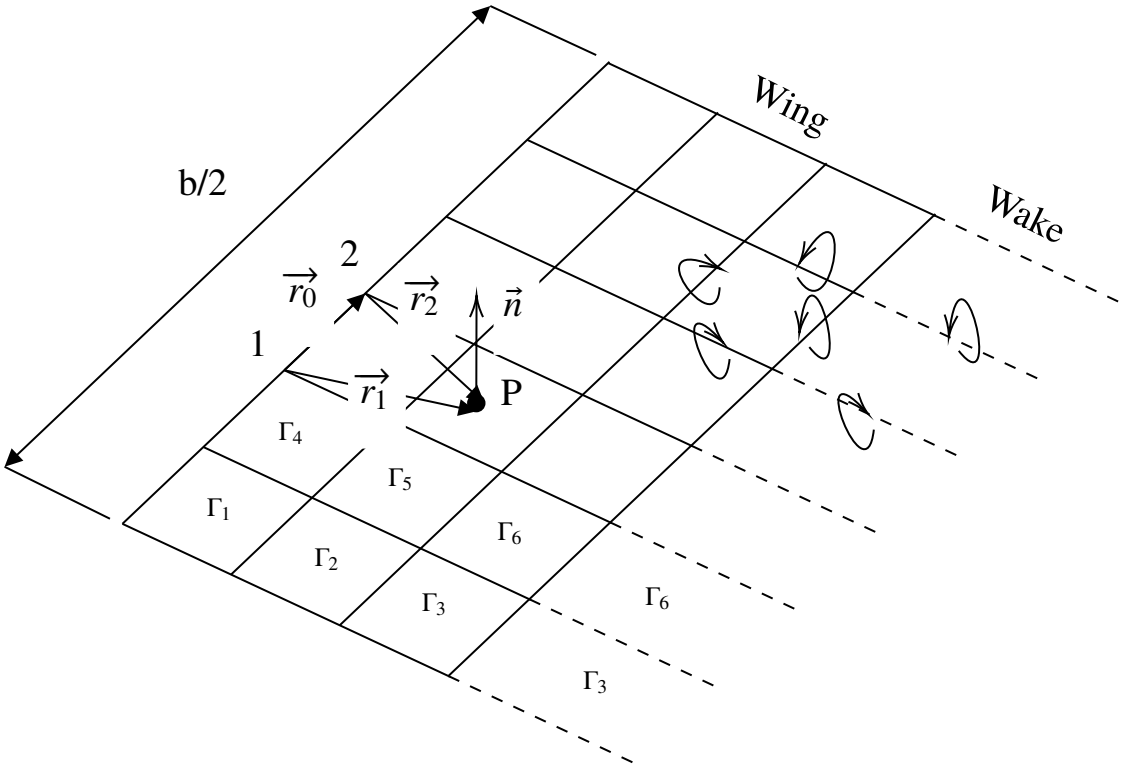

Fig. 1 VLM computational setup.

Using these assumptions, a modified influence matrix $\boldsymbol{A'}$ can be computed with the influence coefficient :

$$A'_{a,b} = \sum_{k=-\infty}^{\infty} A_{a,b+kN} \tag{13}$$

Since the influence coefficient is proportional to the inverse of the distance between two panels, in practice the values of k can be restricted to a finite number of panels. Finally, by assuming that the wing is infinite the $(kn_j + j)n_i + i$ equations are identical. Hence the problem is restricted to N equations :

$$\begin{bmatrix} A'_{1,1} & A'_{1,2} & \dots & A'_{1,N} \\ A'_{2,1} & A'_{2,2} & \dots & A'_{2,N} \\ \vdots & \vdots & \ddots & \vdots \\ A'_{N,1} & A'_{N,2} & \dots & A'_{N,N} \end{bmatrix} \begin{pmatrix} \Gamma_1 \\ \Gamma_2 \\ \vdots \\ \Gamma_N \end{pmatrix} + \vec{V}_\infty \cdot \vec{n} = 0 \tag{14}$$

To account for viscous and compressibility effects, the Non-Linear Vortex Lattice Method (NL-VLM) [19, 20, 23–25] is used. This method applies a correction to the local angle of attack of the VLM sections in order to get a local lift coefficient $C_{l_{inv}}$ equal to a two-dimensional lift coefficient $C_{l_{vis}}$, which is provided by Reynolds-Averaged Navier-Stokes (RANS) simulations, experimental data, or as in this paper by manufactured lift curves. They are called manufactured lift curves because they are given by an analytical formula chosen to present some specific features. The viscous correction concept is illustrated in fig. 3. Due to the thin airfoil theory the sectional lift coefficient of the VLM is :

$$C_{l_{inv}} = 2\pi\alpha_{inv} \tag{15}$$

$$\alpha_{inv} = \alpha_{3D} + \alpha_i + \Delta\alpha \tag{16}$$

with α_{3D} the geometrical angle of attack, α_i the induced angle of attack and $\Delta\alpha$ the viscous correction. The viscous coupling is done for the spanwise grid section j as :

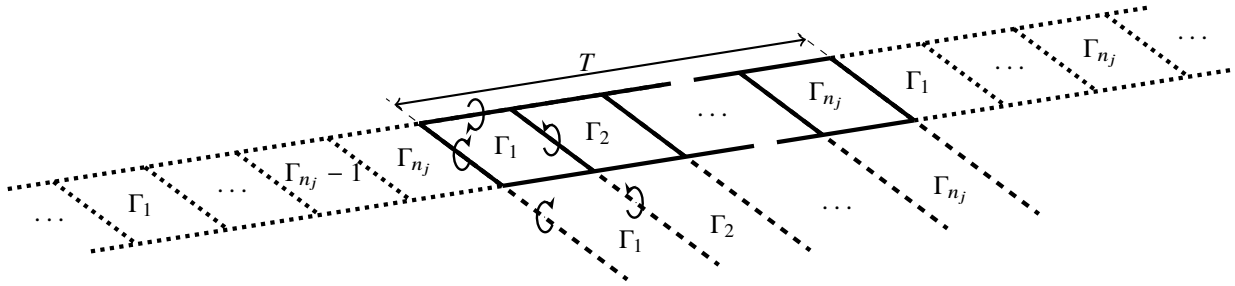

Fig. 2 Infinite wing Vortex Lattice Method with periodicity assumption.

$$\alpha^k_{eff,j} = \frac{C_{l^k_{inv,j}}}{2\pi} - \Delta\alpha^k_j \tag{17}$$

$$\Delta\alpha^{k+1}_j = \Delta\alpha^k_j + \omega\frac{C_{l_{vis}}(\alpha^k_{eff,j}) - C^k_{l_{inv,j}}}{2\pi} - \mu\left(\Delta\alpha^k_{j-1} - 2\Delta\alpha^k_j + \Delta\alpha^k_{j+1}\right) \tag{18}$$

with ω a relaxation factor and μ a dissipation coefficient to smooth the solution in the spanwise direction. $C_{l_{vis}}(\alpha_{eff,j})$ is the lift coefficient provided by a $C_l(\alpha)$ curve to correct the VLM. This lift coefficient relation can vary from one spanwise section to the other. However, for this study, it is assumed to be constant. These equations and the VLM system of equations are coupled and result in a non-linear system. Hence, the $\Delta\alpha$ are first initialized at zero for the first solution of the VLM system to get the $C_{l_{inv}}$ of each section. Then subiterations between the VLM and the coupling are carried out up to the point where $\left|C_{l_{vis}} - C_{l_{inv}}\right| < \epsilon$ with ϵ a given tolerance. $\Delta\alpha$ is added to the VLM as a rotation of the vector $\vec{n}$ normal to the panel. Thus only the right-hand side of the VLM system of equations is modified during subiterations and the influence matrix is inverted only once. The lift polar provided for the viscous coupling can include the post stall angle of attack, thus allowing to model three-dimensional wings in the post-stall regime.

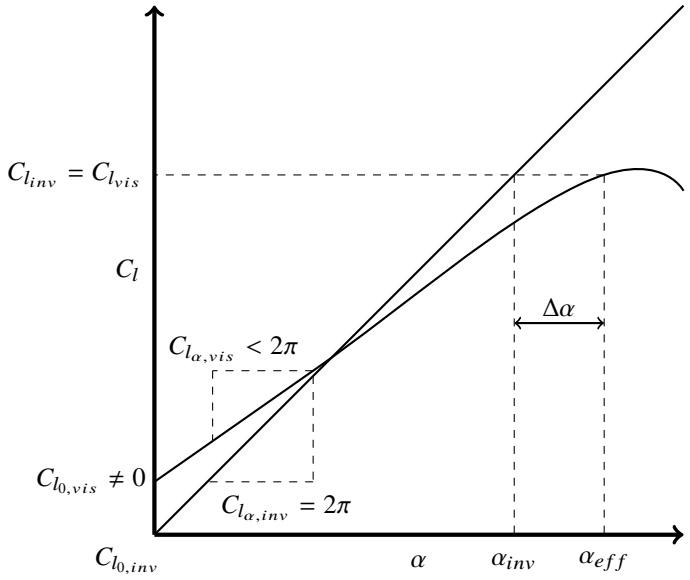

Fig. 3 Viscous coupling applied to the VLM model.

IV. Numerical verification

This section provides numerical verification of the VLM method, in particular with respect to the periodicity assumption and the viscous coupling. A classic test case for a VLM code is the verification that $C_l = 2\pi\alpha$ for a wing of infinite aspect ratio, which is equivalent to a two-dimensional thin airfoil. The same case with the NL-VLM should return the lift of the user provided viscous lift curve. Hence, simulations are carried out for a wing of the aspect ratio 1×10^{12} with 100 panels in the spanwise direction and one panel in the chordwise direction. No artificial dissipation is used. Fig. 4 shows the solution of the VLM and the NL-VLM coupled to the manufactured lift polar proposed by Spalart [15] :

$$C_l(\alpha) = 2\pi\alpha + 0.5(1.2 - 2\pi\alpha)(1 + erf((\alpha - 0.28)/0.02)) \tag{19}$$

One can observe that the linear VLM correctly reproduces the thin airfoil theory with $C_l(\alpha) = 2\pi\alpha$. When this VLM is coupled to a viscous polar, the two-dimensional lift coefficient prescribed by the polar is obtained. Note that the results are matching pre and post-stall regions.

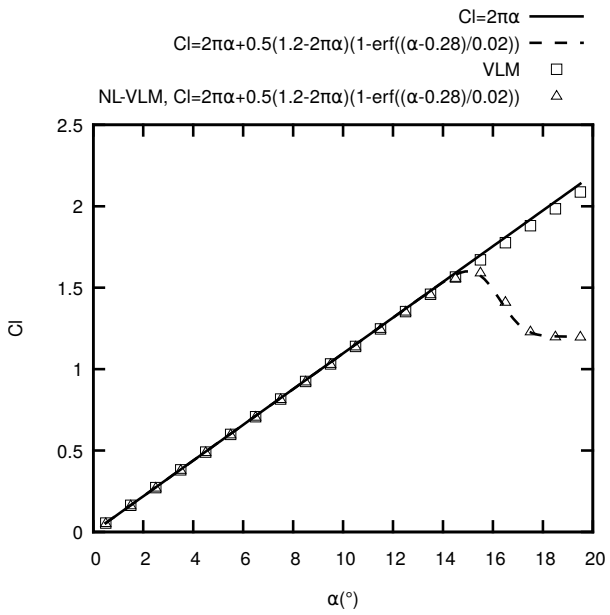

Fig. 4 Infinite wing solution of the NL-VLM

Now that the non-linear coupling is verified, the periodicity assumption should be verified, a nontrivial task. To do so, simulations are carried out on wings with a periodic twist distribution of the form :

$$\alpha_t(y) = \alpha_{t0} + \alpha_{t1} cos(2\pi y/\lambda_t) \tag{20}$$

with α_t the twist, α_{t0} the mean twist, α_{t1} the amplitude of the twist modulation and λ_t the twist period. Wings of large aspect ratio with 1 chordwise cell, a spanwise spacing $\Delta y = 0.1$, $\alpha = 5.0°$, $\alpha_{t0} = 0.0°$, $\alpha_{t1} = 10.0°$ and $\lambda_t = 5.0$ are computed. Fig. 5 shows the lift distribution for wings of aspect ratio 50, 100 and 200. As one can see the solution around $y/c = 0.0$ is nearly periodic, thus it will be used to verify the computation with the periodicity assumption.

Fig. 6 shows the solution of the same problem using the periodicity assumption proposed in this study. The computation is carried out with one ($b/c = 5$) and three ($b/c = 15$) twist periods between the periodicity conditions. The spanwise periodic VLM allows to recover the solution of the large aspect ratio wing, at a significantly lower computational cost since only one and three twist periods are meshed. The lift coefficient with 10 chordwise panels is also shown, which does not change the lift coefficient. Fig. 7 shows the Γ distribution with 1 and 10 spanwise cells. As one can see, the grid has an effect on the Γ distribution but not on the sectional lift distribution.

In conclusion, the proposed NL-VLM model is able to model infinite wing with an assumption on the periodicity of the solution. This method is also able to take into account viscous effects, including the post-stall regime.

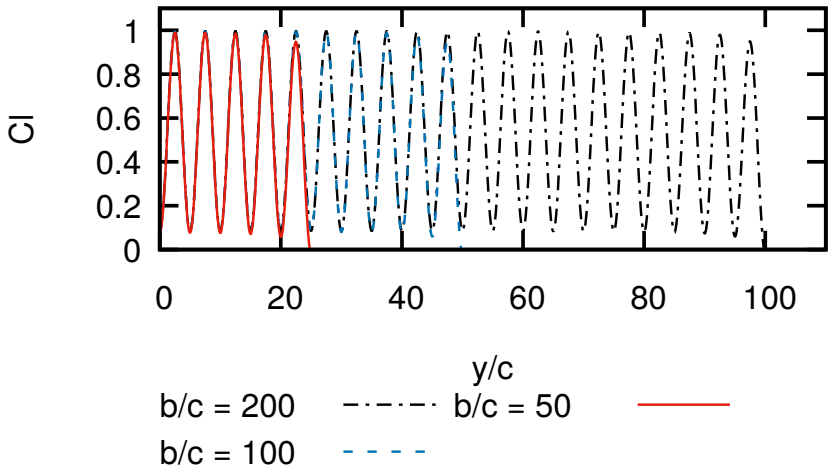

Fig. 5 Effect of the span on the lift distribution of wing with periodic twist.

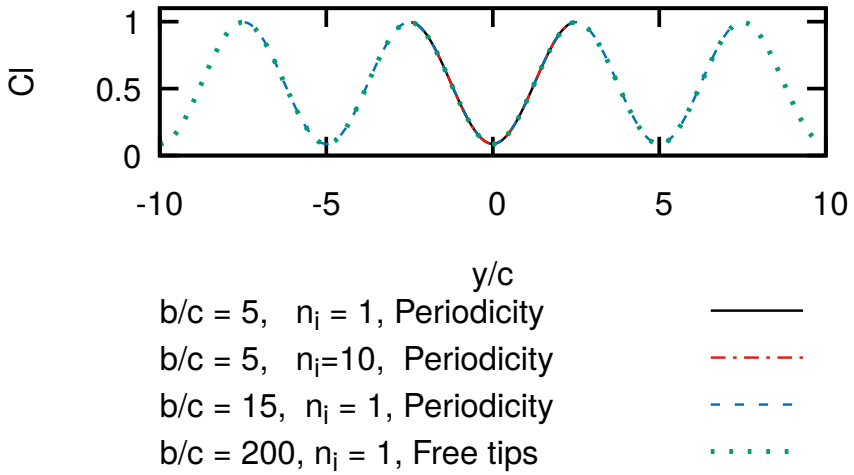

Fig. 6 Solution of the wing with periodic twist using the periodicity assumption.

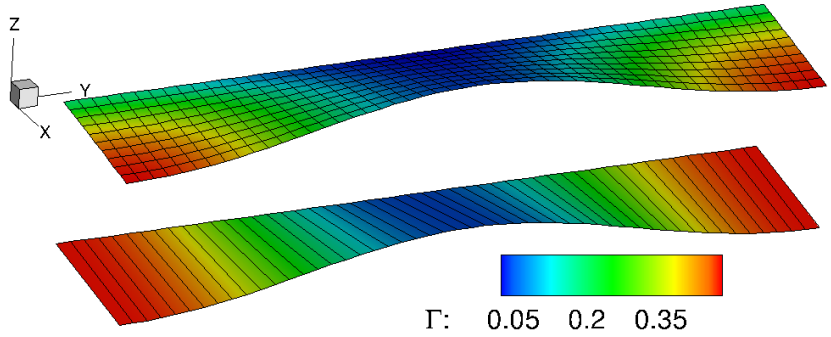

Fig. 7 Circulation distribution over the periodic wing with 1 and 10 chordwise panels.

V. Analysis of the lift cell

A. Lifting line - Infinite Wing

This section investigates the infinite wing lifting line model proposed by Spalart [15]. Fig. 8 shows the lift coefficient and the effective angle of attack used for interpolation in the lift polar proposed by Spalart [15] (eq. 19, polar 1). Two curves are shown for the lift coefficient. One is the lift coefficient interpolated from the lift polar at the effective angle of attack, The other is computed from the circulation Γ computed with the smoothed A_j and B_j Fourier coefficients. This analysis is done for a wing with an aspect ratio of 10, at an angle of attack of 16° and with a filter width $c_f = 0.23$. A thousand points are used to discretize the wing and 200 terms are kept in the Fourier series. The latter is very large considering the fact that the Gaussian filter reduces the impact of modes with high wavenumbers. As one can see, the solution of our implementation reproduces the one of Spalart [15]. However, the Gaussian filter causes a large deviation of the lift coefficient from the one interpolated inside the lift polar. Nonetheless, the global lift coefficient is the same up to 10^{-6}. Hence the filter reduces the sharp features of the lift distribution with a very small impact on the integrated lift force. One can also observe that the minimum lift coefficient is 1.2, which is the asymptotic value of the manufactured lift polar at high angles of attack. For this reason, the effective angle of attack can reach higher values with no effect on the lift coefficient. The maximal sectional lift coefficient corresponds to interpolation in the lift polar at the maximum lift coefficient angle of attack (15°). Hence, with this model the spanwise solution alternates between regions where the lift coefficient is interpolated in the post-stall regime and in the pre-stall regime. The solution is in the stall regime (negative slope of the $C_l(\alpha)$ curve) only for a narrow band of sections.

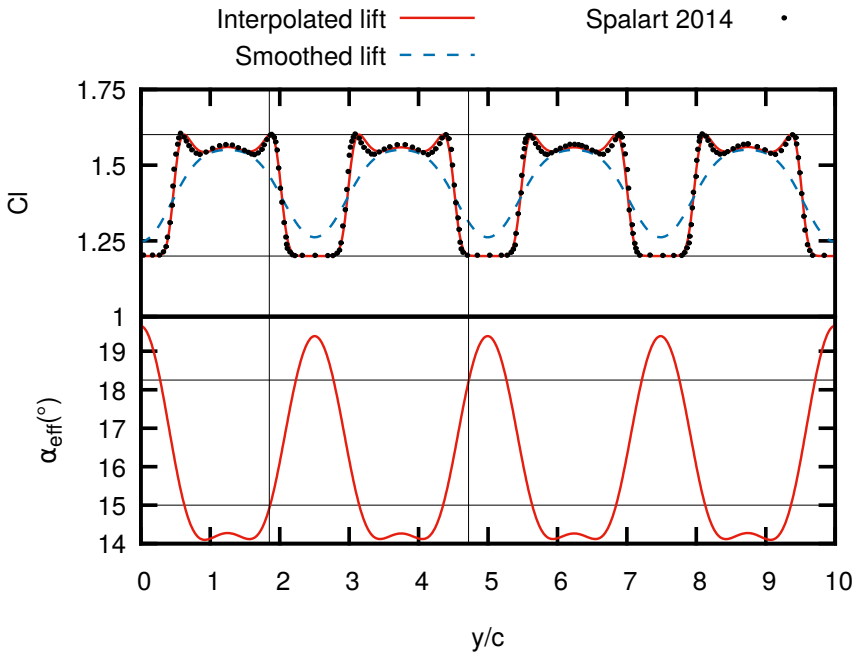

Fig. 8 Lift distribution and effective angle of attack of Spalart's lifting line model.

As stated by Spalart [15] this model has a bias towards the high wavenumber modes. Hence the Gaussian filter is necessary to obtain a converged solution or the number of modes must be limited. Fig. 9 shows the result with several number of Fourier modes and without the Gaussian filter. The lift cells phenomenon is only observed when the number of modes is at least 2. In this case, two cells are obtained. An interesting point is the fact that the number of cells increases with the number of modes and the model bifurcates towards the highest wavenumber possible. For a higher number of modes the model fails to converge without the Gaussian filter. This figure also shows the fact that the lift distribution is smoothed out, even though the Gaussian filter is not used. In fact the Fourier Series is unable to closely follow the Γ distribution. Hence, in the iterative process the Fourier series gives a smooth distribution of w. Then sharp features in the lift distribution are found when interpolating inside the lift polar and fitting a Fourier Series in the Γ

results in a smooth distribution.

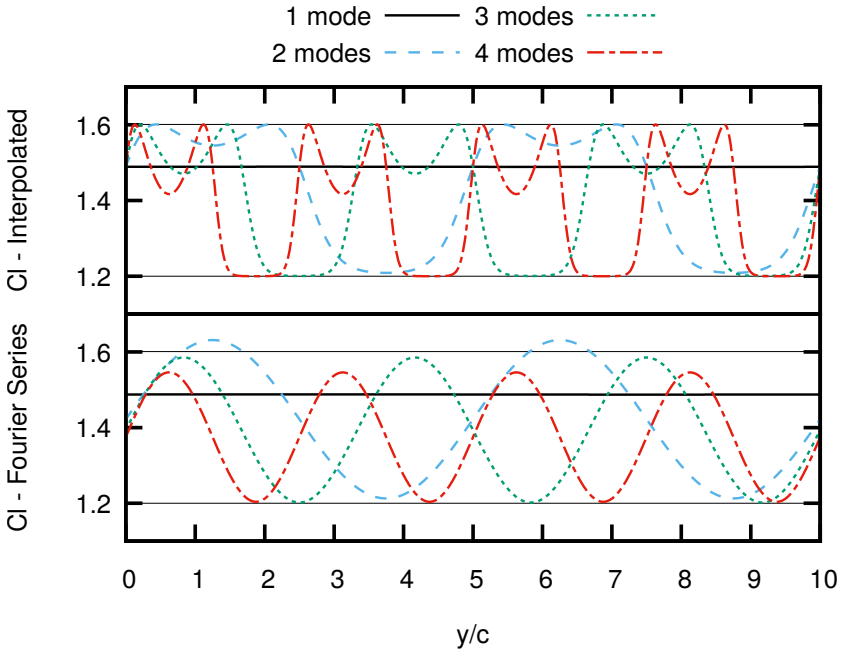

Fig. 9 Lift distribution of Spalart's lifting line model without the Gaussian filter.

As mentioned above, the lift coefficient cannot go below 1.2 in the high effective angle of attack range because it is the asymptotic value of the lift distribution. Test with a polar without an asymptotic value shows the fact that the model cannot stabilize to a steady-state solution if the slope of the lift curve remains negative.

B. Lifting surface - Elliptic wing

To apply the NL-VLM model to a finite wing problem, first the case of a wing with an elliptic chord distribution is investigated. This test case presents the advantage that the downwash should be constant on the wing and thus the effective angle of attack should also be constant. This means that the stall should occur at every wing section simultaneously. The elliptic wing is defined with a unitary chord at the root and the aspect ratio $\lambda = b^2/S_{ref}$. The lift polar used for the viscous coupling is the one given in equation 19. Figs. 10 and 11 shows the effect of the artificial dissipation term on the lift and effective angle of attack distribution respectively. Simulations are done at an angle of attack of 18°. The NL-VLM model is able to converge to a solution in the post-stall regime without adding a dissipation term. However, as one can see in fig. 11, the effective angle of attack of some of the sections is unrealistically large. This is explained by the fact that the lift coefficient provided by the polar is constant for angles of attack higher than 19° (this angle of attack as well as the maximum lift coefficient angle are shown in this graph). Hence, the NL-VLM model can increase the angle of attack correction to impact the linear VLM system of equations without impacting the viscous lift coefficient, which stays constant at 1.2. By comparing fig. 10 and fig. 11, one can observe that the parts of the lift distribution equal to 1.2 correspond to the sections where the effective angle of attack is greater than 19°. The other sections of the wing have an effective angle of attack lower than 15° (the maximum lift coefficient angle). One can also observe that no wing section has an effective angle of attack in the region where C_{l_α} is negative. This means that the parts of fig. 10 where the lift coefficient is between 1.2 and 1.6 are in fact not stalled in the lift polar. This seems to indicate that the NL-VLM model does not allow a wing section to see a negative C_{l_α}. Since an elliptic wing is considered, for which the whole wing stalls together, the NL-VLM forces some section to get un-stalled and other to be fully stalled.

Even though a solution can be obtained without the artificial viscosity term, this term smooth out the sharp discontinuity in the effective angle of attack distribution. The main effect of the smoothing is observed in fig. 11 where the very large effective local angles of attack decrease. As such the smoothing allows to correct the unrealistic effective

angle of attack. As is the case for the lifting line model of Spalart [15], adding this dissipation term creates two spanwise lift distributions. The first one is computed in the VLM system and the second one is the lift coefficient interpolated at the effective angle of attack. This is shown in fig. 12. Without the dissipation, the two ways of computing the lift coefficient return the same result. However, when adding the dissipation, lift distributions with peaks similar to the ones of Spalart [15] are obtained. It is interesting to note that artificial dissipation was added by Chattot [17] as a numerical artifact to stabilize the Γ coupling algorithm without knowing its effect on the stabilization of the physical properties of the flow.

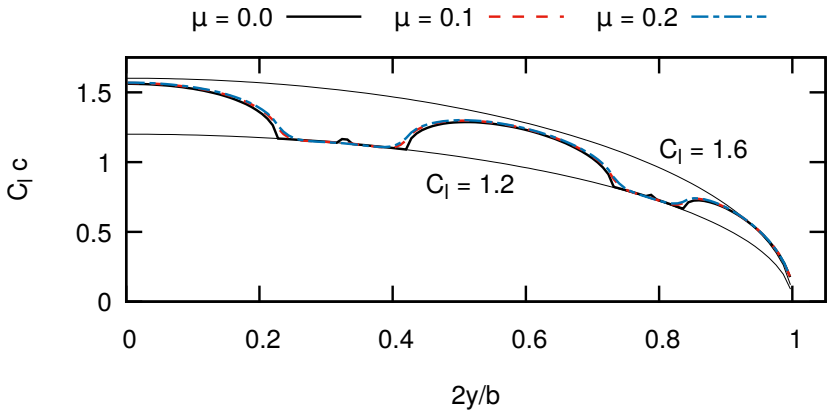

Fig. 10 Effect of the dissipation coefficient μ on the lift distribution (elliptic wing, $\lambda = 16.0$, $\alpha = 18°$, polar 1).

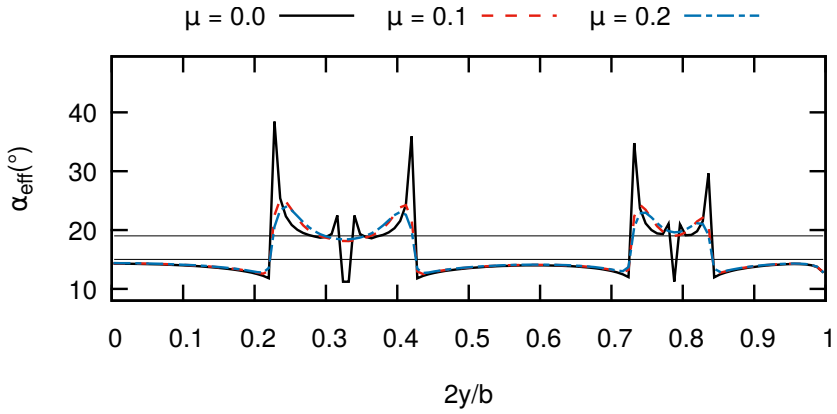

Fig. 11 Effect of the dissipation coefficient μ on the effective angle of attack (elliptic wing, $\lambda = 16.0$, $\alpha = 18°$, polar 1).

Fig. 13 shows the distribution of the circulation Γ on wings at several angles of attack and using an artificial dissipation with $\mu = 0.2$. The wing is in the pre-stall regime for the angle of attack of 17° because the downwash causes the wing to be at a constant effective angle of attack lower than 15°. One can observe the cellular patterns in the solution for the angle of attack of 18° and 19°. For the angle of attack of 20°, the cells no longer occur because the wing is completely stalled. Fig. 14 shows the distribution of the lift coefficient multiplied by the local chord for several aspect ratios and geometrical angles of attack. The lift coefficient is multiplied by the local chord to highlight the elliptic distribution of the lift force. As one can see, the elliptic lift distribution is obtained for low aspect ratios and low angles of attack. For the other aspect ratios, lift cells are observed. This is caused by the fact that the downwash is constant along the span and stronger for the lower aspect ratios. Thus, the wings with a low aspect ratio reach the stall condition at a higher angle of attack. Two curves are used to highlight the boundaries of the region of the local lift polar where C_{l_α} is negative ($C_l = 1.2$ and $C_l = 1.6$). As soon as the effective angle of attack becomes higher than the maximum lift

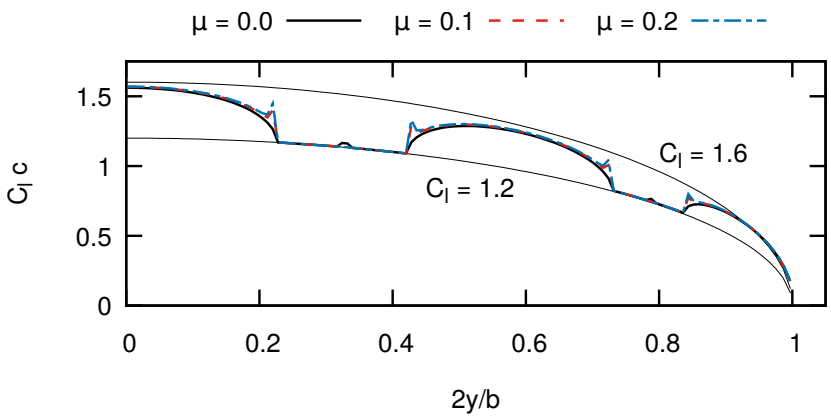

Fig. 12 Effect of the dissipation coefficient μ on the lift coefficient interpolated at the effective angle of attack (elliptic wing, $\lambda = 16.0$, $\alpha = 18°$, polar 1).

coefficient angle, lift cells occur. Also, the number of cells increases with the aspect ratio. When the wings of aspect ratio 16 and 20 reach the stall conditions they respectively have 3 and 4 lift cells. Hence, the variation of the number of cells appears to increase linearly with the aspect ratio for angles of attack slightly past the maximum lift coefficient angle. As the angle of attack is further increased the lift cells break down into smaller cells, up to the point where the wing is fully stalled and $C_l c = 1.2$ (the asymptotic value of the manufactured lift polar) for the entire wing.

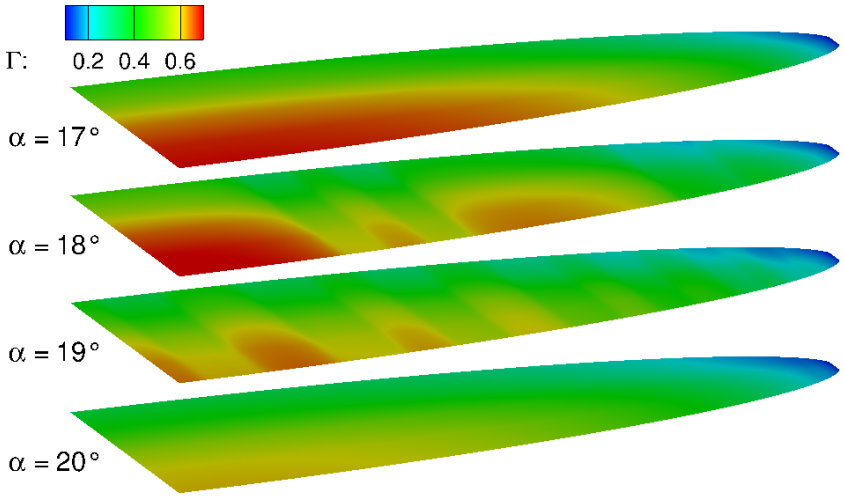

Fig. 13 Circulation distribution at several angle of attack (elliptic wing, $\lambda = 16.0$, polar 1).

The lift polar is another variable in the NL-VLM model. To characterize this effect, one can design a series of lift polar with different post-stall behavior based on the formulation of Spalart [15] :

$$C_l(\alpha) = C_{l\alpha,0}\alpha + 0.5(C_{l0} - C_{l\alpha,1}\alpha)(1 + erf((\alpha - \alpha_0)/\alpha_1)) \tag{21}$$

with the parameters given in table 1. Fig. 15 shows these lift polars. The polar 2 is designed to remove the asymptotic behavior of the original lift polar (polar 1). The polar 3 is selected to increase the negative slope of the lift polar, while the polars 4 and 5 decrease this slope.

Figs. 16 and 17 show the lift coefficient and the effective angle of attack computed with this selection of lift polars. In every case the grid is refined in both topological directions to obtain a grid independent solution and the size of the mesh changes from one case to the other. As one can see by comparing the solutions with the polar 1 and 2, adding a positive slope as the angle of attack goes to infinity helps to remove the non-physically large effective angles of attack,

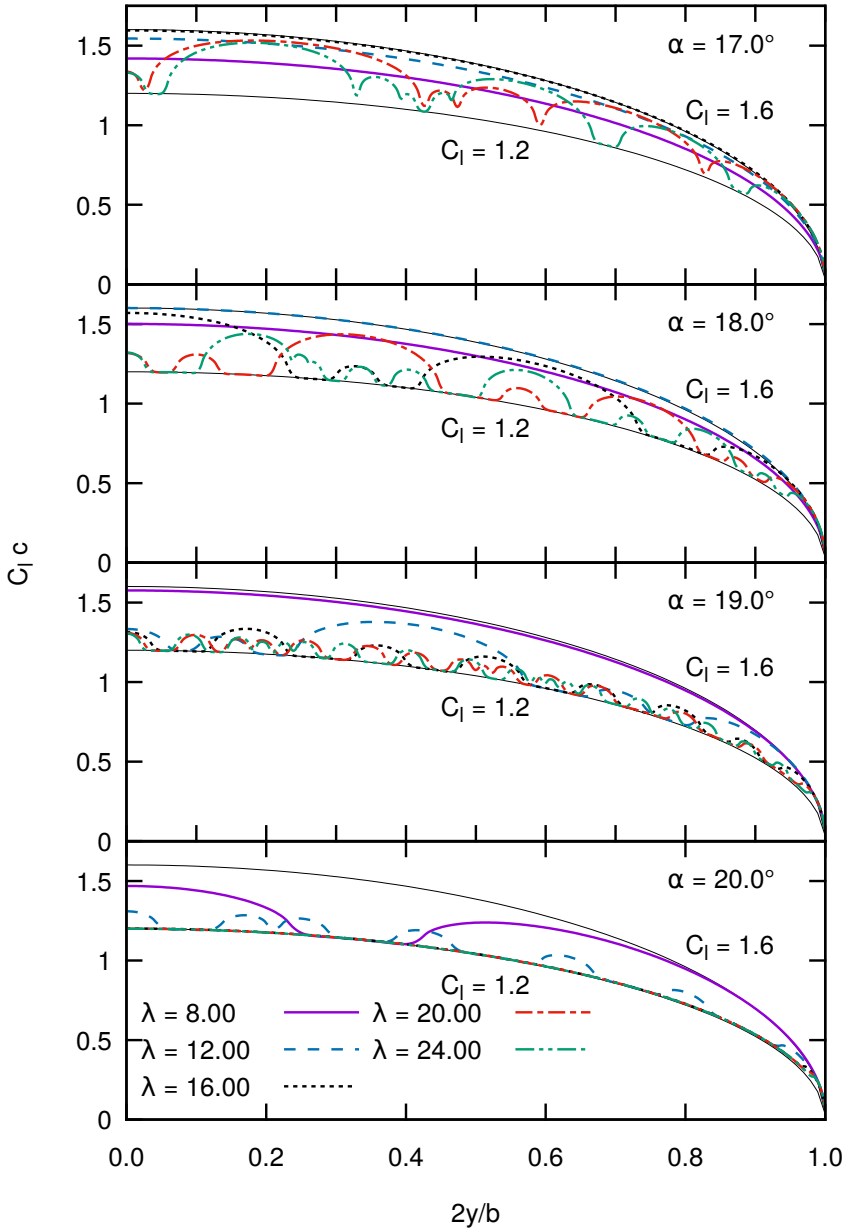

Fig. 14 Lift coefficient distribution of several aspect ratios at several angles of attack (elliptic wing, polar 1).

which is an effect similar to adding the artificial dissipation. However, this does not change the number of lift cells and significantly affect the amplitude of the latter. This further emphasizes the fact that having $C_{l_\alpha} = 0$ causes the viscous correction and the VLM system of equation to become decoupled. On the other hand, changing the slope of the lift polar in the post stall regime significantly changes the number of cells. Decreasing this slope increases the number of cells, while increasing it decreases the number of cells. The criterion found by Gross et al. [16] predict that the wavelength of the cells increases with the norm of the lift slope, if the latter is negative. This tendency is the same as the one observed here. Another interesting point is the fact that a typical leading edge stall will exhibit a sharp reduction of the lift coefficient for angles of attack just past the maximum lift angle. This could be assimilated to an infinite slope which will result in very large wavelengths. Moreover, the range of angles of attack for which the stall cells are observed

Polar	C_{l0}	α_0	α_1	$C_{l\alpha,0}$	$C_{l\alpha,1}$
Polar 1	1.20	0.28	0.02	2π	2.0π
Polar 2	0.72	0.28	0.02	2π	1.5π
Polar 3	0.72	0.28	0.01	2π	1.5π
Polar 4	0.72	0.28	0.03	2π	1.5π
Polar 5	0.72	0.28	0.04	2π	1.5π

Table 1 Parameters of the lift polar.

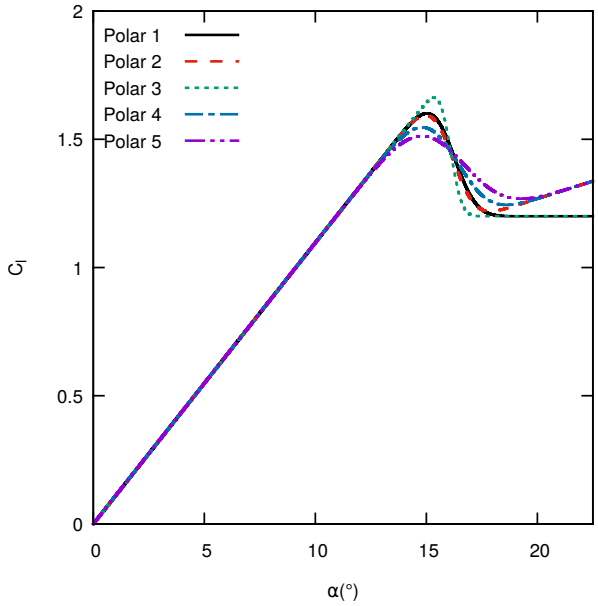

Fig. 15 Selection of manufactured lift curves.

requires the effective angle of attack to be in the negative C_{l_α} area. This region of the lift curve becomes smaller as the lift slope is increased. If this region becomes infinitely small, the elliptic wing will jump from the pre-stall regime to the post-stall one without the occurence of the stall cells phenomenon. This can explain the fact that the stall cells are usually observed for wings with a trailing edge type of stall which is characterized by lift curves similar to the one used in this paper, as reported by Broeren and Bragg [5].

C. Lifting surface - Rectangular Wing

Rectangular wings with a Clark Y airfoil section and free tips were studied by Winkelmann and Barlow [3]. To compare with them, the case of a rectangular wing is now studied with the lift polar 5 of the previous section. The simulations are done with a symmetry plane at the root, 8 cells in the chordwise direction and a spanwise grid spacing of $0.025c$. Fig. 18 shows the solution at an angle of attack of 18.4° for aspect ratios of 3, 6, 9 and 12. As observed by Winkelmann and Barlow [3] the number of lift cells is proportional to the aspect ratio of the wing. However, the aspect ratio of 3 is small for a Vortex Lattice Method and no cells are observed. For the other aspect ratios the number of cells is lower than the one observed by Winkelmann and Barlow [3], who clearly had 2 cells for an aspect ratio of 6, while only one is observed here. This discrepancy can be explained by the lift polar used in the NL-VLM. For this reason, a new lift polar is designed to reproduce the experimental lift polar of the Clark Y airfoil at a Reynolds number of 400 000 [26]. The parameter of the manufactured lift polar are selected to reproduce the $C_{l_{max}}$ and early post-stall behavior. The lift polar is extended and a positive slope is added in the high angle of attack range, to get a better conditioning of the NL-VLM. The new lift curve is (polar 6) :

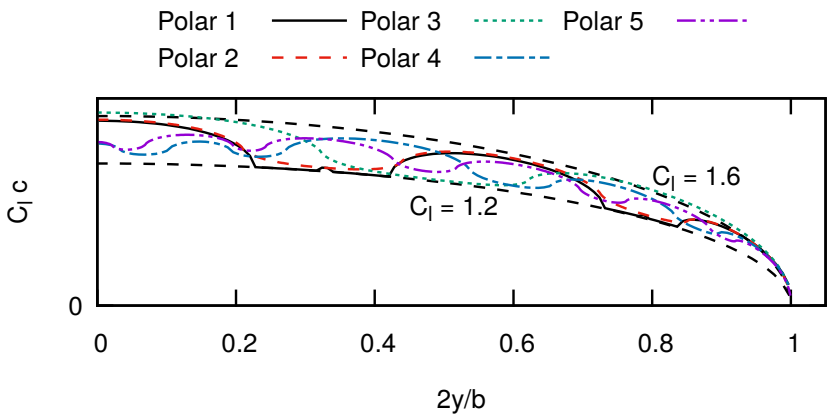

Fig. 16 Effect of the lift polar on the lift distribution (elliptic wing, $\lambda = 16.0$, $\alpha = 18°$).

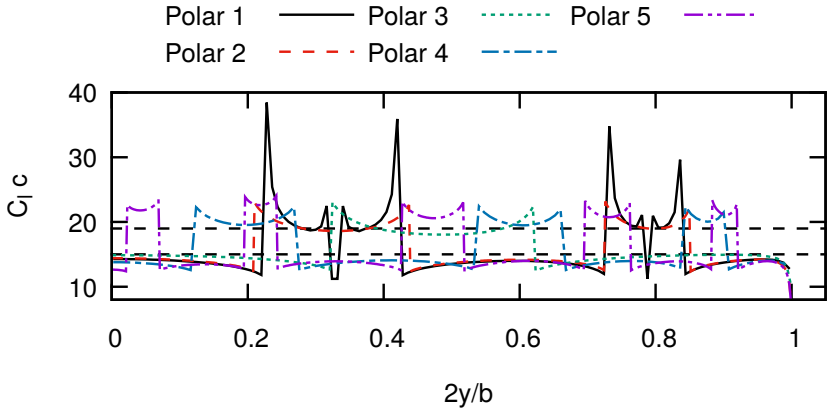

Fig. 17 Effect of the lift polar on the effective angle of attack (elliptic wing, $\lambda = 16.0$, $\alpha = 18°$).

$$C_l(\alpha) = 0.35 + 1.8\pi\alpha + 0.5(0.22 - 1.6\pi\alpha)(1 + erf((\alpha - 0.28)/0.15)) \tag{22}$$

This lift curve is shown in fig. 20 and the spanload of the rectangular wings at an angle of attack of 18.4° (the same as in the experiments of Winkelmann and Barlow [3]) is shown in fig. 21. The number of cells is reported in table 2. The values obtained with this new polar are closer to the experimental one. This confirms that the lift polar is the main parameter which has an influence on the solution of the NL-VLM and that the phenomenon observed in the experiment is linked to an instability present in an inviscid model.

D. Lifting surface - Infinite wing

Finally, the solution of the lifting surface model with the hypothesis of periodicity in the spanwise direction is investigated. Fig. 22 shows the effect of the angle of attack on the solution for a meshed domain of a span of 2. This figure shows the solution with a mesh of 101 by 1 cells and the influence matrix is built using 300 periods on both sides of the simulated domain. The lift polar 5 of table 1 is used. This case reproduces an infinite wing. Hence, as long as the solution stays two-dimensional the induced angle of attack is zero and the wing will stall at the same angle of attack as the one of the prescribed lift polar. As one can see, the solutions of fig. 22 are two-dimensional for angles of attack below the stall angle (15°) and at very high angles of attack (greater than 19°). In both conditions $C_{l_\alpha} > 0$. For angles of attack between these two values, stall cells occur. Hence, the stall cells occur in cases where $C_{l_\alpha} < 0$. However, the solution is not periodic within the computational domain. This is explained by the fact that the periodicity assumption is only imposed between the two edges of the computational domain. Thus, the interior of the domain remains free.

λ	Winkelmann and Barlow [3]	Polar 5	Polar 6
3	1	0	0
6	2	1	2
9	3 to 5	2	5
12	5 to 6	4	7

Table 2 Number of stall cells compared to the experiments.

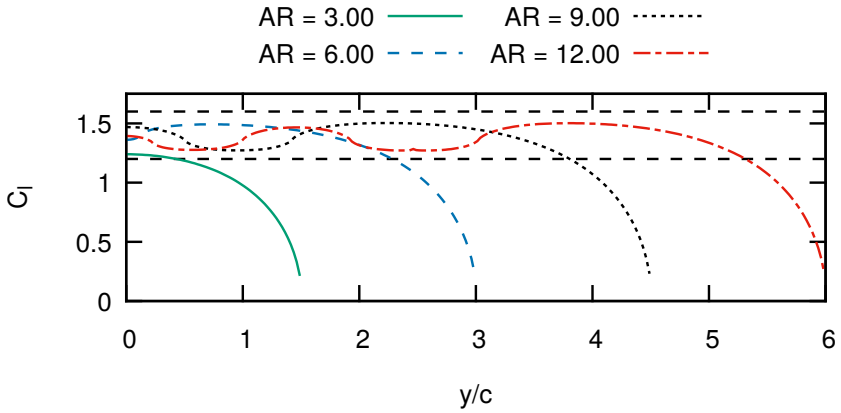

Fig. 18 Effect of the aspect ratio on the lift coefficient distribution (rectangular wing, $\alpha = 18.4°$, polar 5).

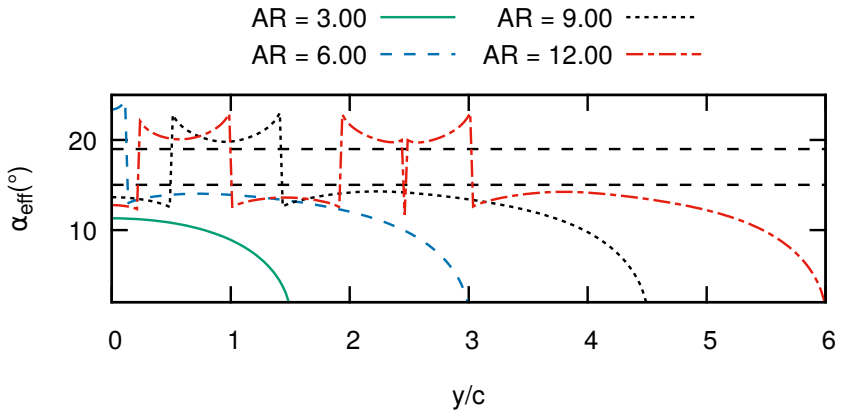

Fig. 19 Effect of the aspect ratio on the effective angles of attack (rectangular wing, $\alpha = 18.4°$, polar 5).

Moreover, multiple solutions cannot be ruled out. Fig. 23 shows the effective angle of attack distribution for these cases. As was observed previously, there is no section with an effective angle of attack where C_{l_α} is negative. The polar used has a positive slope as the angle of attack goes to infinity. For this reason, the effective angle of attack remains in a realistic range.

A free parameter of the model is the number of periods considered in the infinite wing assumption. The greater this number, the smaller are the influence coefficients which are neglected in the infinite wing assumption. Fig. 24 shows the effect of this parameter for the same case. One can observe that the number of periods must be greater than 100 to remove the truncation effect, and a constant solution is obtained if one refines this parameter. A study of the mesh refinement in the spanwise direction has been carried out, with no significant variation on the solution.

One can now study the effect of the size of the computational domain on the lift cells. To do so, the span of the domain is increased and the number of grid cells is increased to keep the size of the grid cells constant. The number

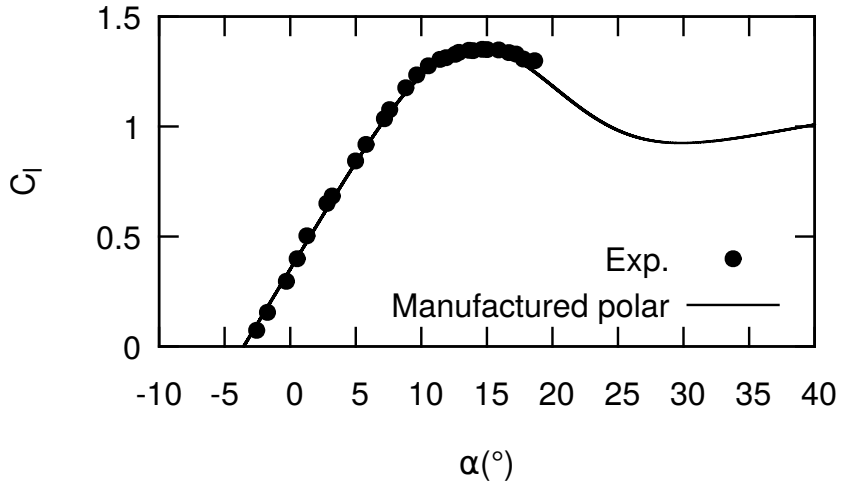

Fig. 20 Manufactured lift curve for the Clark Y airfoil based on the experiments [26].

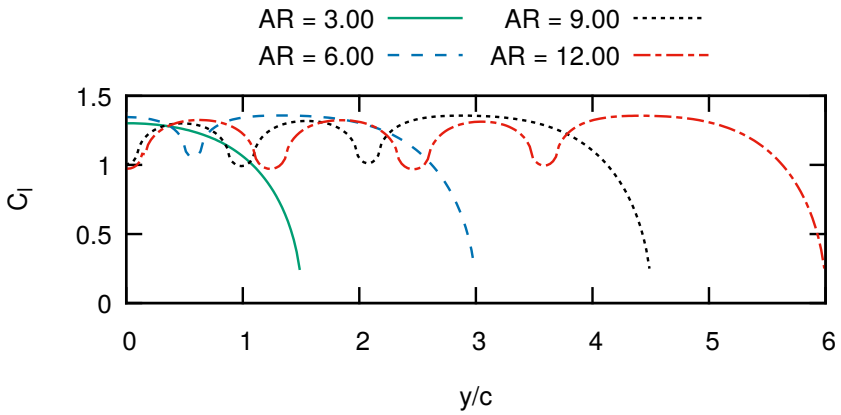

Fig. 21 Effect of the aspect ratio on the lift coefficient with the experimental lift curve (rectangular wing, $\alpha = 18.4°$, polar 6).

of periodicity is adapted to keep the neglected influence coefficients at a distance of $600c$. This criterion is selected because the influence coefficients decay with the distance and using a constant number of periodicity would result in a large computational cost for the larger mesh, since the influence coefficients of these cells must be computed. Fig. 25 shows the effect of the aspect ratio. As expected the number of lift cells increases with the aspect ratio. This relation is linear. However, when the aspect ratio is high, the solution becomes noisy in the middle of the computational domain. This effect remains unexplained.

Finally, one can add the artificial viscosity term. This effect is shown in fig. 26 and 27. As it was the case for the finite wing, this parameter has the effect of smoothing out the effective angle of attack and the lift distribution but the solution remains similar.

VI. Conclusion

A lifting surface model is applied towards the study of stall cells, thereby extending the lifting line model of Spalart [15]. To this end, the non-linear Vortex Lattice Method proposed by Gallay and Laurendeau [19] is used. Contrary to the model of Spalart, this model does not use a spectral transformation so that solutions can be non-periodic within the bound of the computational domain. This lifting surface model uses an α-based coupling with a lift polar to include viscous and compressibility effects and an artificial viscosity is added to smooth out discontinuity in the

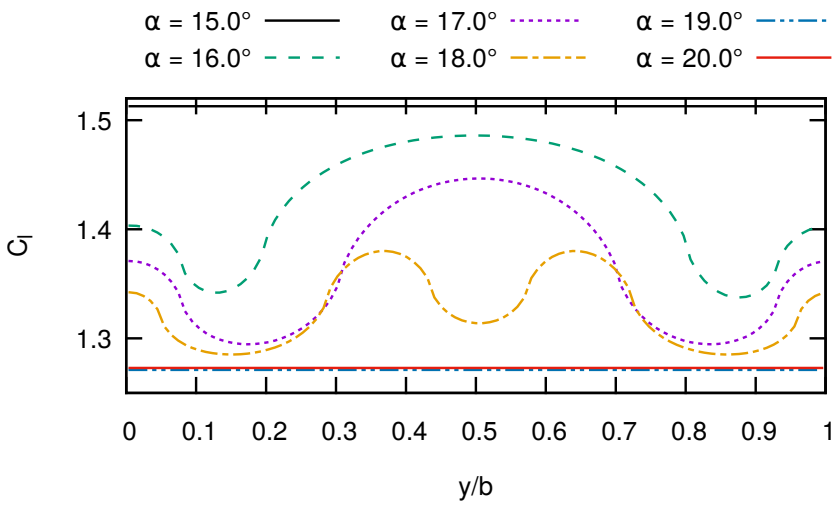

Fig. 22 Effect of the angle of attack on the lift distribution (infinite wing, $\lambda = 2.0$, polar 5).

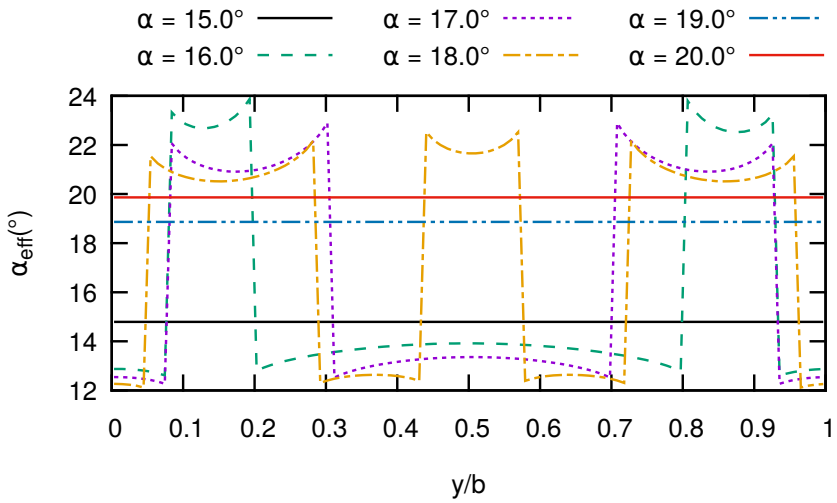

Fig. 23 Effect of the angle of attack on the sectional effective angle of attack distribution (infinite wing, $\lambda = 2.0$, polar 5).

solution. The NL-VLM model is first verified and characterized for canonical cases. In particular, the paper introduces a mathematical modification to compute infinite wings by including a periodicity condition. This allows to simulate infinite wings with a spanwise grid refinement sufficient to simulate phenomenon with a size of the order of the chord length. The case of elliptic, rectangular and infinite wings in the post-stall regimes are analyzed. For all these cases, an instability is observed as soon as the slope of the lift versus angle of attack relation is negative. This behavior is expected from the analyses presented by Spalart [15] and Gross et al. [16]. Contrary to the model of Spalart, which requires the use of a smoothing factor to obtain a converged solution, the NL-VLM converges to a solution without adding the artificial dissipation. Adding this term smooths out the solution, but does not change the number of stall cells. Another observation is the fact that adding a dissipation to the NL-VLM model results in two lift distributions. The first one being the one of the viscous coupling and the other the one of the inviscid model. Without dissipation, these two lifts are the same. A similar behavior is observed with the model of Spalart. Finally, solutions are in qualitative agreement to the results of Winkelmann and Barlow [3] on a rectangular wing without the need of adding any particular filter. The lifting surface model allows to include parameters like the sweep angle, taper ratio and twist. As such, this model provides a low-cost model for the prediction of the wavelength of the stall cells, which could be used in wing design.

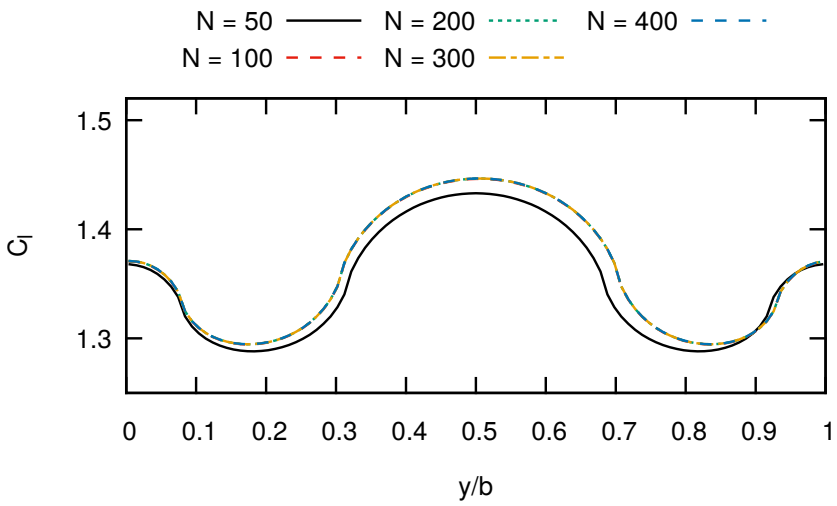

Fig. 24 Effect of the number of spanwise period on the lift distribution (infinite wing, $\lambda = 2.0$, polar 5).

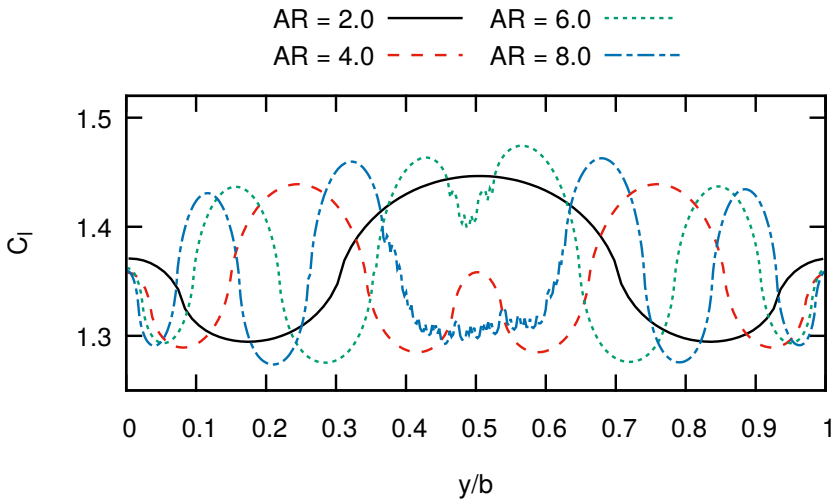

Fig. 25 Effect of the aspect ratio on the lift distribution (infinite wing, polar 5).

Acknowledgment

This work is financially supported by the Natural Sciences and Engineering Research Council of Canada (NSERC), the Canada Research chair Programs and Office National d'Études et de Recherches Aérospatiales (ONERA).

References

[1] Moss, G. F., and Murdin, P. M., "Two-Dimensional Low-Speed Tunnel Tests on the NACA 0012 Section Including Measurements Made During Pitching Oscillations at the Stall," Tech. rep., Aeronautical Research Council, 1971.

[2] Gregory, N., Quincey, V. G., O'Reilly, C. L., and Hall, D. J., "Progress Report on Observations of Three-Dimensional Flow Patterns Obtained during Stall Development on Aerofoils, and on the Problem of Measuring Two-Dimensional Characteristics," Tech. rep., Aeronautical Research Council, 1971.

[3] Winkelmann, A. E., and Barlow, J. B., "Flowfield Model for a Rectangular Planform Wing beyond Stall," *AIAA Journal*, Vol. 18, No. 8, 1980, pp. 1006–1008. doi:10.2514/3.50846.

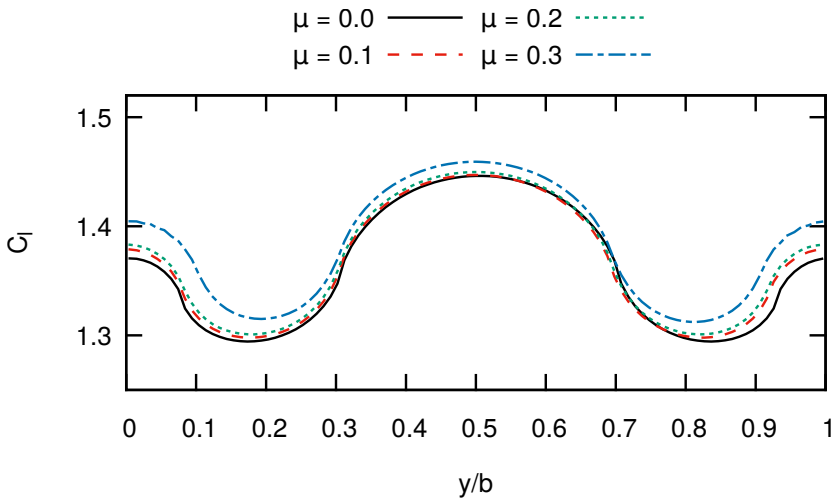

Fig. 26 Effect of the artificial dissipation on the lift distribution (infinite wing, $\lambda = 2.0$, polar 5).

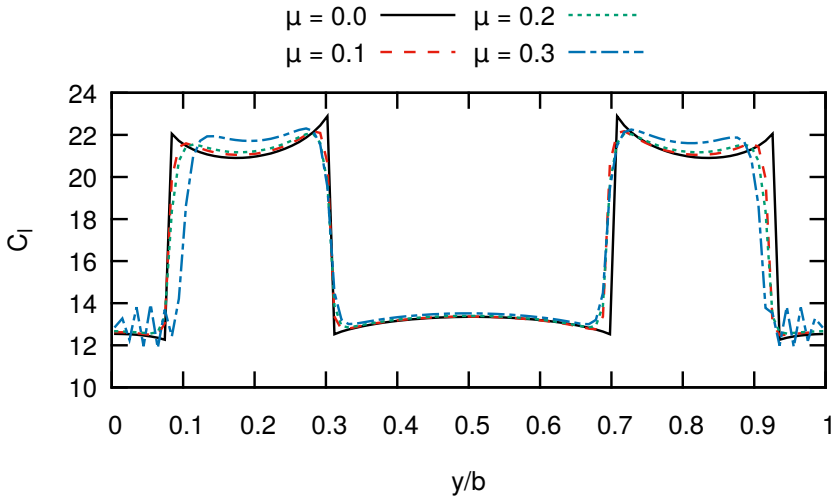

Fig. 27 Effect of the artificial dissipation on the effective angle of attack distribution (infinite wing, $\lambda = 2.0$, polar 5).

[4] Schewe, G., "Reynolds-Number Effects in Flow around More-or-Less Bluff Bodies," *Journal of Wind Engineering and Industrial Aerodynamics*, Vol. 89, No. 14-15, 2001, pp. 1267–1289. doi:10.1016/S0167-6105(01)00158-1.

[5] Broeren, A. P., and Bragg, M. B., "Spanwise Variation in the Unsteady Stalling Flowfields of Two-Dimensional Airfoil Models," *AIAA Journal*, Vol. 39, No. 9, 2001, pp. 1641–1651. doi:10.2514/2.1501.

[6] Dell'Orso, H., and Amitay, M., "Parametric Investigation of Stall Cell Formation on a NACA 0015 Airfoil," *AIAA Journal*, Vol. 56, No. 8, 2018, pp. 1–13. doi:10.2514/1.J056850.

[7] Manni, L., Nishino, T., and Delafin, P.-L., "Numerical Study of Airfoil Stall Cells Using a Very Wide Computational Domain," *Computers & Fluids*, Vol. 140, 2016, pp. 260–269. doi:10.1016/j.compfluid.2016.09.023.

[8] Bertagnolio, F., Sørensen, N. N., and Rasmussen, F., "New Insight Into the Flow Around a Wind Turbine Airfoil Section," *Journal of Solar Energy Engineering*, Vol. 127, No. 2, 2005, pp. 214–222. doi:10.1115/1.1861927.

[9] Plante, F., Dandois, J., and Laurendeau, É., "Similarities Between Cellular Patterns Occurring in Transonic Buffet and Subsonic Stall," *AIAA Journal*, Vol. 58, No. 1, 2019, pp. 1–14. doi:10.2514/1.J058555.

[10] Kitsios, V., Rodríguez, D., Theofilis, V., Ooi, A., and Soria, J., "BiGlobal stability analysis in curvilinear coordinates of massively separated lifting bodies," *Journal of Computational Physics*, Vol. 228, No. 19, 2009, pp. 7181–7196. doi:10.1016/j.jcp.2009.06.011.

[11] Rodríguez, D., and Theofilis, V., "On the Birth of Stall Cells on Airfoils," *Theoretical and Computational Fluid Dynamics*, Vol. 25, 2011, pp. 105–117. doi:10.1007/s00162-010-0193-7.

[12] He, W., Gioria, R. S., Pérez, J. M., and Theofilis, V., "Linear Instability of Low Reynolds Number Massively Separated Flow around Three NACA Airfoils," *Journal of Fluid Mechanics*, Vol. 811, 2017, pp. 701–741. doi:10.1017/jfm.2016.778.

[13] Zhang, W., and Samtaney, R., "BiGlobal linear stability analysis on low-Re flow past an airfoil at high angle of attack," *Physics of Fluids*, Vol. 28, No. 4, 2016. doi:10.1063/1.4945005.

[14] Plante, F., Dandois, J., Beneddine, S., Sipp, D., and Laurendeau, É., "Numerical Simulations and Global Stability Analyses of Transonic Buffet and Subsonic Stall," *54 Th 3AF International Conference on Applied Aerodynamics*, FP63-AERO2019-plante, 2019.

[15] Spalart, P. R., "Prediction of Lift Cells for Stalling Wings by Lifting-Line Theory," *AIAA Journal*, Vol. 52, No. 8, 2014, pp. 1817–1821. doi:10.2514/1.J053135.

[16] Gross, A., Fasel, H. F., and Gaster, M., "Criterion for Spanwise Spacing of Stall Cells," *AIAA Journal*, Vol. 53, No. 1, 2015, pp. 272–274. doi:10.2514/1.J053347.

[17] Chattot, J.-J., "Analysis and Design of Wings and Wing/Winglet Combinations at Low Speeds," AIAA Paper 2004-0220, 2004. doi:10.2514/6.2004-220.

[18] van Dam, C. P., "The aerodynamic design of multi-element high-lift systems for transport airplanes," *Progress in Aerospace Sciences*, Vol. 38, No. 2, 2002, pp. 101–144. doi:10.1016/S0376-0421(02)00002-7.

[19] Gallay, S., and Laurendeau, E., "Nonlinear Generalized Lifting-Line Coupling Algorithms for Pre/Poststall Flows," *AIAA Journal*, Vol. 53, No. 7, 2015, pp. 1784–1792. doi:10.2514/1.j053530.

[20] Gallay, S., and Laurendeau, E., "Preliminary-Design Aerodynamic Model for Complex Configurations Using Lifting-Line Coupling Algorithm," *Journal of Aircraft*, Vol. 53, No. 4, 2016, pp. 1145–1159. doi:10.2514/1.C033460.

[21] Paul, R. C., and Gopalarathnam, A., "Iteration Schemes for Rapid Post-Stall Aerodynamic Prediction of Wings Using a Decambering Approach," *International Journal for Numerical Methods in Fluids*, Vol. 76, No. 4, 2014, pp. 199–222. doi:10.1002/fld.3931.

[22] Katz, J., and Plotkin, A., *Low-Speed Aerodynamics*, 2nd ed., Cambridge University Press, Cambridge, 2001. doi:10.1017/CBO9780511810329.

[23] Kontogiannis, A., Parenteau, M., and Laurendeau, E., "Viscous-Inviscid Analysis of Transonic Swept Wings using 2.5D RANS and Parametric Shapes," AIAA Paper 2019-2116, 2019. doi:10.2514/6.2019-2116.

[24] Parenteau, M., Sermeus, K., and Laurendeau, E., "Viscous-Inviscid Analysis of Transonic Swept Wings using 2.5D RANS and Parametric Shapes," AIAA Paper 2018-1049, 2018. doi:10.2514/6.2018-1049.

[25] Parenteau, M., Laurendeau, E., and Carrier, G., "Combined high-speed and high-lift wing aerodynamic optimization using a coupled VLM-2.5D RANS approach," *Aerospace Science and Technology*, Vol. 76, 2018, pp. 484–496. doi:10.1016/j.ast.2018.02.023.

[26] Lyon, C., Broeren, A. P., Giguère, P., Gopalarathnam, A., and Selig, M. S., "Summary of Low-Speed Airfoil Data," Tech. rep., University of Illinois, 1997.